Photonic-Enabled Beam Switching Mm-Wave Antenna Array

Alvaro José Pascual-Gracia, Muhsin Ali, Thomas Batte, Fabien Ferrero, Laurent Brochier, Olivier de Sagazan, Frederic van Dijk, Luis Enrique Garcia Munoz, Guillermo Carpintero, Ronan Sauleau, et al.

Photonic-Enabled Beam Switching Mm-Wave Antenna Array

Álvaro J. Pascual, Muhsin Ali, Thomas Batté, Fabien Ferrero, Laurent Brochier, Olivier de Sagazan, Fréderic van Dijk, Luis E. García Muñoz, Guillermo Carpintero Del Barrio, Ronan Sauleau, *Fellow, IEEE,* and David González-Ovejero, *Senior Member, IEEE*

***Abstract*—We present a photonically-excited antenna array at E-band for scanning by beam switching in wireless links. First, we discuss the proposed technique applied to photonic-enabled (sub)millimeter-wave transmitters. Next, we present our implementation; it consists of two sub-arrays of stacked patches as primary feeds of a Polytetrafluoroethylene (PTFE) lens, with one photodiode feeding each sub-array. To validate the assembly, the return loss and radiation patterns have been measured for one of the sub-arrays excited with a coplanar probe. In turn, the lens illuminated by one of the sub-arrays yields a directivity of 27 dBi. The radiation patterns measured for the transmitter module (including the lens) are in very good agreement with full-wave simulations, and they show that excitation of one of either sub-arrays allows beam switching between $\pm 2.7^{\circ}$ with a beam crossover at $-3\,\mathrm{dB}$. Finally, we have tested the transmitter in a 0.6 m wireless link. Depending on the position of the detector and on which sub-array is excited, we have accomplished 5 Gbps transmission for on-off-keying modulation and direct detection (BER $= 10^{-11}$). The system constitutes an initial proof of photonic-assisted beam switching for mm-wave transmitters enabling broadband operation with a directive and switchable beam.**

***Index Terms*—Antenna array, beam steering, beam switching, E-band, mm-wave, photomixing antenna, wireless communications**

I. Introduction

THE increasing demand for data traffic in wireless systems will require the deployment of high capacity cellular networks. Millimeter- (mm-) and sub-millimeter (sub-mm) waves have been widely accepted as the most suitable spectral regions to provide enough bandwidth for multi-Gbps data throughput [1]–[3]. In particular, the E-band (71-76 and 81-86 GHz) constitutes one promising band. It has been already allocated for fixed cellular backhaul links [4]. The E-band offers a $2 \times 5\,\mathrm{GHz}$ bandwidth not intensively licensed so far [5] and lies within a relatively low atmospheric absorption window of approximately 0.5 dB/km [6].

On the other hand, intense research efforts carried out over the past decades have put the photonic generation of mm- and sub-mm waves in the spotlight. Specifically, the possibility of seamless integration of photonic transmitters (Tx) with fiber optics has led to numerous point-to-point wireless links demonstrations [7]–[10]. The photonic approach is advantageous in terms of antenna remoting, centralization of signal processing with flexible modulation formats, wavelength division multiplexing for multichannel wireless links, and compatibility with already deployed and forthcoming optical access networks. With a bandwidth spanning over 4 THz, photonic generation and analog signal processing of mm-waves can benefit from ultra-broadband, reliable, and cost-effective commercial components such as Er-doped fiber amplifiers (EDFAs), which are nearly insensitive to the mm-wave frequency. However, photonic Tx provide lower source power than their electronic counterparts, suffering from a large down-conversion loss at the O/E converter (usually a high-speed photodiode). This shortcoming, in addition to a high free space loss at mm-waves, requires the use of line-of-sight links and highly directive antennas.

An additional challenge is to provide photonic-enabled mm-wave transmitters with beam steering capabilities. This feature is also crucial to enable high data rate wireless links in realistic scenarios [11]–[14]. Some relevant use cases include fine alignment of highly directive beams [10], compensation from twists and sways from mounting structures [15], [16], and reconfigurable links [13], [17].

Despite the numerous demonstrations of photonic-enabled wireless links, experimental realizations of photonic Tx featuring beamsteering at E-band frequencies or beyond are relatively uncommon. Only in recent years the number of experimental realizations has started to grow [18]–[23], although the performance assessment in a wireless link still has received little attention [21]. In [19], beam steering was

Á. J. Pascual, O. de Sagazan, R. Sauleau, and D. González-Ovejero are with Univ Rennes, CNRS, IETR (Institut d'Électronique et des Technologies du numéRique) – UMR 6164, F-35000, Rennes, France.
M. Ali, L. E. García Muñoz, and G. Carpintero Del Barrio are with Universidad Carlos III de Madrid, 28911 Leganés, Spain.
T. Batté is with Institut Foton, INSA (National Institute of Applied Science) – UMR 6082, Rennes, France.
F. Ferrero and L. Brochier are with Université Côte d'Azur, CNRS, LEAT (Laboratory of Electronics Antennas and Telecommunications) – UMR 7248, 06903 Sophia Antipolis, France.
F. van Dijk is with III-V lab, a joint laboratory between Nokia Bell Labs France, Thales Research and Technology France, and CEA-LETI, 91767 Palaiseau, France.
Corresponding author: Á. J. Pascual alvaro-jose.pascual@univ-rennes1.fr

Á. J. Pascual, R. Sauleau, and D. González-Ovejero would like to thank the European Union financement through the European Regional Development Fund (ERDF), and the French region of Brittany, Ministry of Higher Education and Research, Rennes Métropole and Conseil Départemental 35, through the CPER Project SOPHIE / STIC & Ondes. This work has received a French government support granted to the Labex CominLabs excellence laboratory and managed by the National Research Agency in the "investing for the future" program under reference ANR-10-LABX-07-01.
Digital Object Identifier XXXXXXXXXXXXXXXXXXX.

demonstrated but the antenna radiated into a high permittivity substrate ($\epsilon_r = 11.9$), which caused an early onset of grating lobes. In [21], a 4×1 horn antenna array was used, but the resulting array yielded a gain of $18\,\mathrm{dBi}$, and the waveguide-based feeding structure may be impractical to scale for arrays with higher gain. In [18], the difficulty to efficiently illuminate several elements led to a 1×3 array of active antennas with a reduced gain. All the examples above have in common a small number of active elements, up to four. The reason is the difficulty of integrating a large number of photomixers with the antennas while maintaining optimal optical illumination. This issue has hindered the development of wireless links with phased arrays featuring a high gain and beam steering simultaneously.

An approach that combines a switched-beam antenna with quasi-optical (QO) elements to obtain the required gain enhancement can be a plausible solution to obtain a directive but also steerable beam. In particular, we propose in this work photonic-assisted beam switching with a mm-wave antenna array integrated with uni-travelling-carrier photodiodes (UTC-PDs). By using a lens, the Tx features a highly directive and switchable beam, while a low number of active components need to be integrated. The system constitutes a proof-of-concept towards photonic-enabled mm- or sub-mm wave Tx featuring broadband operation with a directive and switchable beam.

The remainder of the manuscript is organized as follows: Section II explains the proposed photonic-enabled beam switching scheme. Section III describes the design, assembly, and characterization of a 2×1 antenna array used as a lens primary feed for beam switching. Next, Section IV describes the experimental characterization of photonic beam switching. Section V presents the system performance in a wireless data transmission experiment. Finally, the conclusions are provided in Section VI.

II. Photonic-Enabled Beam Switching

In this section, we describe the proposed mm-wave Tx with beam switching capabilities. It is to be observed that this scheme is quite different from beam switching schemes based on circuit [24]–[26] or quasi-optical [27]–[29] beam formers, which are often used in antenna systems to obtain a discrete number of progressive phase differences for the elements of an antenna array. Fig. 1 shows the block diagram of the corresponding architecture. First, the optical tones modulated according to a data string are carried by an optical fiber. Then, the optical input is directed to one of the N elements by an optical switch. Next, the light illuminates a PD connected to the antenna that will radiate the modulated mm-wave carrier. Finally, it would also be possible to integrate HEMT amplifiers after the photodiodes to enhance the emitted power, as in [10]. For beam switching, the antennas are located at the back focal plane of a lens with focal length f, as shown in Fig. 1. When the antenna is placed at a distance s out of the optical axis, the beam tilt is given from geometrical optics by

$$\tan\theta = \pm s/f, \tag{1}$$

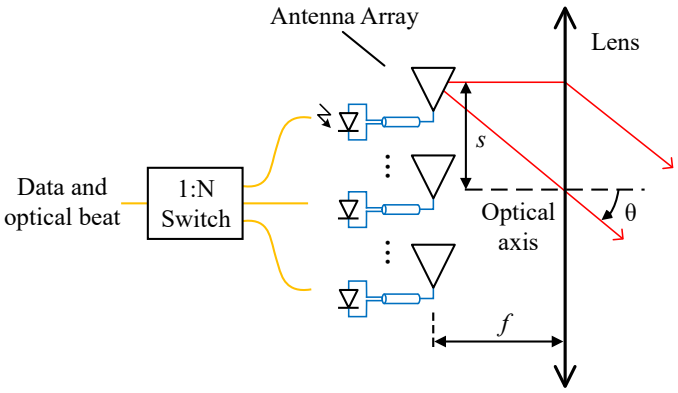

Fig. 1. Architecture of a mm-wave antenna array excited photonically for beam switching.

where θ is the angle measured with respect to broadside, and the sign depends on the clockwise direction of θ. In this case, only one element is active at a time, and the beam can be switched among N different directions given by (1). The scanning properties of dielectric lenses have been studied in [30]. In general, lens systems present field of views narrower than phased arrays [31], but the proposed architecture fully serves for beam alignment purposes in point-to-point links [10], [11].

The beam switching technique applied to a photonic-enabled mm-wave transmitter presents several trade-offs that make it a very interesting route to explore. First, it is possible to achieve a high directivity (measured $> 32\,\mathrm{dBi}$) [4], [32] due to the lens, which does not depends on the number of elements, N. In principle, N can be low, and given the cost of III-V components [12], it is desirable to use as few as possible to fulfill the system requirements. In practice, this will depend on the desired field of view of the transmitter, so the technique is very well suited to applications where only a few beam directions are required, e.g., to compensate misalignment between the emitter and the receiver in point-to-point links.

Even if beam switching allows discrete scanning directions only (64 beam directions in [4]), the element separation can be chosen to obtain a beam crossover at $-3\,\mathrm{dB}$ for quasi-continuous coverage, with other levels also possible [33]. Last, the beam orientation is simply controlled by a optical switch with fast switching time, low insertion loss (30-300 ns and 2 dB, respectively, for the 1×4 Agiltron NanoSpeed switch [34]), and low power consumption. It is worth noting that mechanical steering [35] could be an alternative to the scheme in Fig. 1. In this case, the lens or the antenna would move to shift the emitter position with respect to the optical axis, thus leading to a continuous beam steering. However, the movement velocity ($10\,\mathrm{mm/s}$ in [35, Section 2.1.1], equivalent to $\approx 10^\circ\,/\mathrm{s}$) produces a steering much slower than the proposed optical switching scheme, which would not be in general enough to comply with latency and reliability requirements in telecommunications applications. Finally, beam switching does not provide power combining, so this technique relies more heavily on amplifiers to enhance the emitted power and in turn increase the link distance.

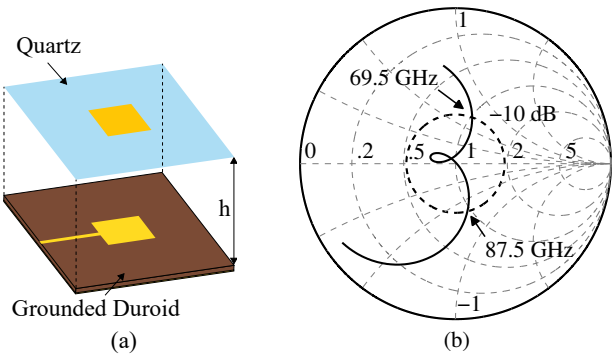

Fig. 2. (a) Primary array element composed of a stack of two patches. (b) Corresponding Smith chart.

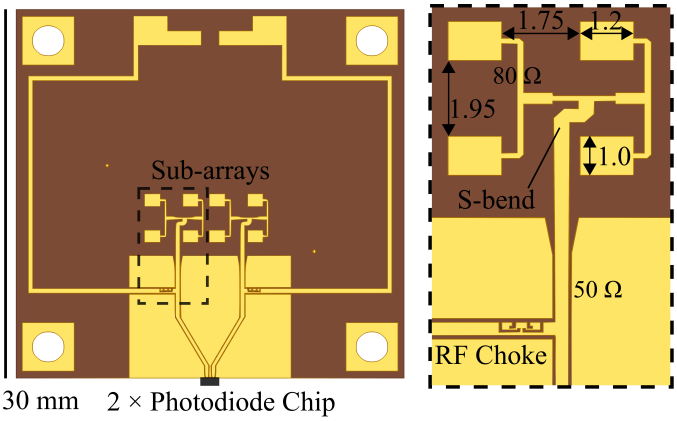

Fig. 3. Left: designed PCB on Duroid 5880 (VIAS not shown). Right: detailed view of one of the sub-arrays (dimensions in mm). The width and length of the top patches are 1.2 mm and 1.075 mm, respectively.

III. Antenna Array

In this section, we describe the design and assembly of the antenna array used as primary feed of a dielectric lens. For validation, we also show measurements of the radiation pattern and return loss of a prototype excited with a ground-signal-ground (GSG) probe. The array has been fabricated using printed circuit board (PCB) technology on a 127 μm-thick, high-frequency Duroid 5880 laminate ($\epsilon_r = 2.24$, $\tan\delta = 0.004$ at 60 GHz) [36].

A. Design

The design of the transmitter has been carried out with High Frequency Structure Simulator (ANSYS HFSS, release 19.0.0) [37] and starts with the optimization of the array element. The array element should feature large gain and impedance bandwidth to provide the desired channel capacity. Radiation should be directed towards one half-space, and the element should be sufficiently small to enable the array configuration.

Microstrip stacked patch antennas are good candidates to fulfill the aforementioned requirements [38], [39]. This approach usually consists in using a driven patch and a coupled parasitic patch with similar dimensions placed at a certain height h from the driven patch, as shown in Fig. 2a. The overall structure presents two close resonances, thereby enhancing the impedance bandwidth of the single microstrip patch. Besides, the extended coupled cavity in the vertical direction does not increase the area of the element and maintains a fairly symmetric radiation pattern and the phase center, which are desirable characteristics for array configurations used as primary feed in a QO system.

In this case, the bottom patch is directly printed on the PCB whereas the top patch is printed on the bottom side of a 112 μm-thick quartz superstrate layer. Quartz exhibits low loss ($\tan\delta < 0.0004$ at 30 GHz [40]), relatively low ϵ_r (≈ 3.80), and is optically transparent. Therefore, alignment marks on both the PCB and the quartz enable an accurate alignment of the layers. The distance h between the top and the bottom patches is controlled by a silicon spacer (shown later), which can be thinned until the desired height. For $h = 300\,\mu$m, a proper balance of coupling between patches is achieved. The relative bandwidth is 23% for a reflection coefficient below -10 dB, as shown in Fig. 2b. The bottom patch is excited by an $80-\Omega$ microstrip line, since it allows better impedance matching to the stacked patches.

Once the stacked patch has been designed, it is replicated to form two 2×2 sub-arrays, as observed in Fig. 3. For each sub-array, a feed network divides the incoming signal from the $50-\Omega$ microstrip line into the four $80-\Omega$ microstrip lines that feed each of the patches. The 2×2 sub-array features a more directive beam, and the patch spacing has been selected to obtain symmetrical patterns along the E- and H-planes. The separation between sub-arrays is 5 mm as is most convenient for beam switching (explained later). The main dimensions of the structure are given in Fig. 3.

The next design step is the the feed network between the antenna array and the source. In this case, the antenna array is excited by a 2×1 UTC-PD chip on InP [41], [42, Fig. 6]. Each UTC-PD feeds independently one of the sub-arrays.

Regarding the feed network connecting the photodiodes with the antenna, a tapered transition is first used to adapt the coplanar waveguide (CPW) output from the photodiodes grown on InP to the Grounded-CPW (GCPW) on Duroid. Next, both signal lines separate to reach the distance required to feed the 2×2 sub-arrays. Perpendicular to the signal lines, one can also observe in Fig. 3 the RF chokes made of split-ring resonators as in [43], and the DC interconnections used to bias the photodiodes. These chokes feature an isolation higher than 20 dB on the whole E-band. Last, transitions from GCPW to microstrip line are used to excite the corporate feed network of each sub-array.

B. Assembly

An aluminum housing has been fabricated to assemble the structure. It holds the PCB and quartz superstrate, provides a groove to place the UTC-PDs chip, and enables DC electrical connections, as shown in Fig. 4.

The first step of the assembly is gluing the thin PCB to the housing using an Ag-based epoxy (EPO-TEK). This avoids the PCB from bending due to temperature changes, which could impact the bonding of the UTC-PDs. Next, the silicon

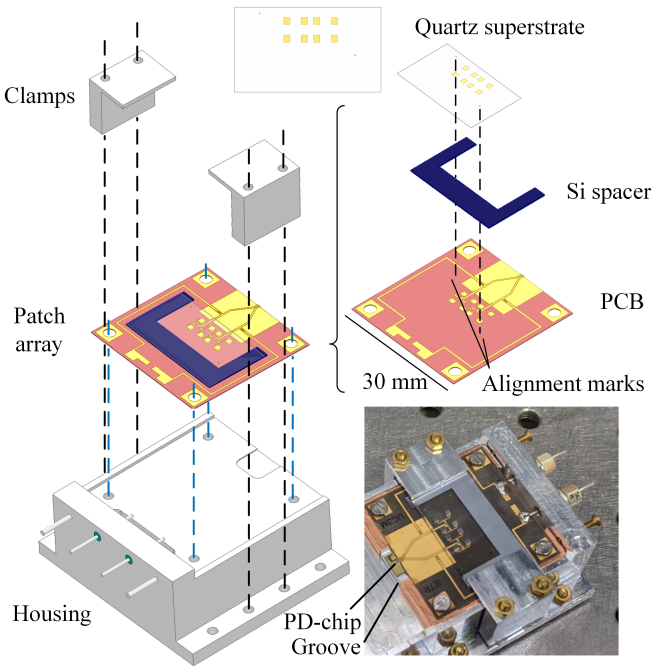

Fig. 4. Top: exploded view of the assembled prototype, and bottom-right: photograph of the prototype.

spacer and quartz superstrate are positioned, as detailed in the exploded view of Fig. 4. The silicon spacer is laser-cut from a standard wafer of thickness $306\,\mu\mathrm{m}$, which is close enough to the nominal value and it does not require to be thinned. As for the top patches and alignment marks on quartz, they are formed using photolithography by a $1\,\mu$m-thick gold layer plus a $50\,\mathrm{nm}$ Ti adhesion layer. To position the quartz precisely, a micropositioner is used to align the marks in the PCB and quartz layers. Next, two lateral clamps are fixed to hold the structure in place. The lateral accuracy achieved is better than $20\,\mu\mathrm{m}$ whereas the in-plane alignment tolerance estimated from full-wave simulations is around $\pm 150\,\mu\mathrm{m}$.

Finally, the last step of the assembly consists in bonding the UTC-PDs electrical output to the PCB. The PD chip is fixed to an AlN block for simpler handling and heat dissipation. In turn, the AlN block is positioned on the housing groove so that the electrical lines of the CPW on InP and the GCPW on Duroid are aligned. It is then fixed to the housing with a UV-curable glue (Blufixx MGS). Next, to perform the bonding, an Ag-based conductive epoxy thread is used. It results in a thick thread ($\approx 60\,\mu\mathrm{m}$ diameter), reducing the bond inductance as compared to wire bonding [42]. The process was demonstrated and explained in more detail in [42], [44]. The assembled structure is shown on the bottom-right of Fig. 4. The grey color of the patches on quartz is due to the titanium layer.

C. Characterization

To validate the prototype, we have measured the return loss and radiation pattern of a single 2×2 sub-array excited by a coplanar GSG probe (Form Factor ACP 110-T), as shown in Fig. 5. The GSG probe was connected to a W-band (75 GHz to 110 GHz) extension head (OML V10VNA2),

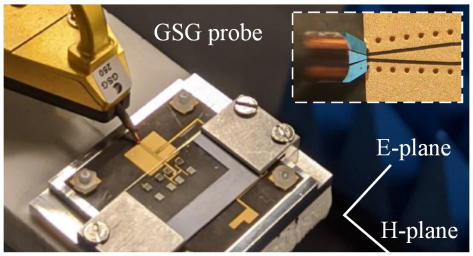

Fig. 5. Detail of the assembled prototype for excitation with a coplanar GSG probe.

in turn connected to a Vectorial Network Analyzer (Agilent N5242A).

Fig. 6a shows the measured and simulated values of the reflection coefficient of the structure shown in Fig. 5. The continuous black line refers to the measurement when the probe is de-embedded using the procedure described in [42]. In a nutshell, the procedure consists in measuring S_{11} with the probe for an open, short, and $\lambda/4$-translated short, all in GCPW, using the same interconnection between the probe and the antenna (shown in the inset of Fig. 5), and on the same PCB substrate as the antenna. After, the transmission matrix of the probe plus its interconnection with the antenna is de-embedded from the measurement. The measured reflection coefficient shows a good agreement with the simulated values in the frequency range that can be tested with the available W-band mm-wave extension head and probe. Discrepancies between simulated and de-embedded curves are attributed to an inaccurate determination of PCB substrate parameters: ϵ_r and thickness (variations within 10% [45]), as well as to tolerances in the PCB manufacturing process and to errors associated with the de-embedding procedure. To illustrate this, the dashed grey line of Fig. 6a shows the simulated results for a deviation in ϵ_r of 0.04 from the nominal value ($\epsilon_r = 2.28$). This deviation could in part explain the horizontal shift between the simulated and the measured curves for the highest values of S_{11} near 84 GHz. For the antenna integrated with the UTC-PDs, the simulated values of $|S_{11}|$ are close to the ones obtained for the single sub-array prototype, below $-10\,\mathrm{dB}$ between $70.1 - 84.7\,\mathrm{GHz}$ with a maximum of crosstalk of $-15\,\mathrm{dB}$ (the UTC-PDs are simulated as lumped sources of $50\,\Omega$ impedance, with the structure detailed in [42]).

To measure the radiation pattern of the prototype (without PTFE lens), a receiving horn (connected to a second W-band extension head), and a 3-D spherical scanner were used. Fig. 6b shows the measured and simulated normalized directivity at $80\,\mathrm{GHz}$. The relatively high side-lobe at $-50°$ occurs due to radiation leakage from the S-bend of the $50-\Omega$ microstrip line that feeds the sub-array (visible in Fig. 3). The side-lobe level stays below $-10\,\mathrm{dB}$ up to $83\,\mathrm{GHz}$. In the measurements, the ripples in the curves are due to the interference coming from the probe tip. Also, it is not possible to measure beyond $45°$ in the H-plane because the probe and mm-wave head block the movement of the 3-D scanner. Finally, the measured cross-polarization levels are $< -15\,\mathrm{dB}$ at broadside. Using the procedure reported in [42], it is also possible to obtain

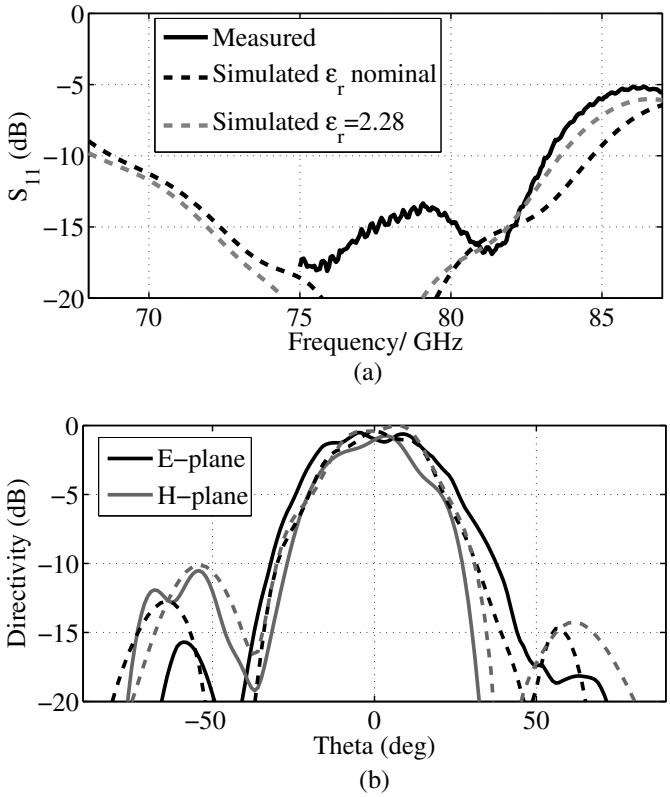

Fig. 6. (a) Magnitude of the reflection coefficient of the prototype. Dashed line: simulated values, continuous line: measured after de-embedding the GSG probe with the procedure outlined in [42]. (b) Normalized directivity at the E- and H-planes for 80 GHz. Continuous line: measured values, and dashed line: simulated values.

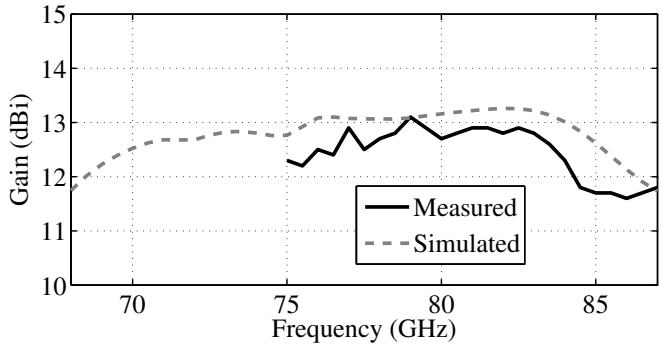

Fig. 7. Simulated and measured gain of the prototype.

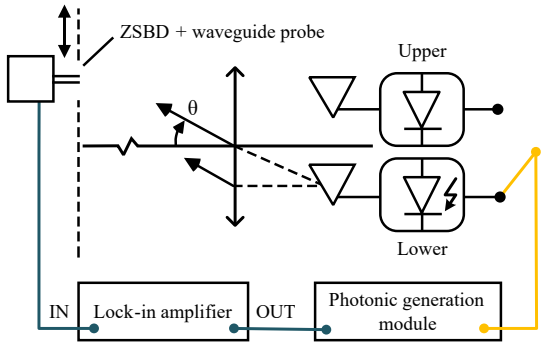

Fig. 8. Schematic of the set-up used to characterize beam switching.

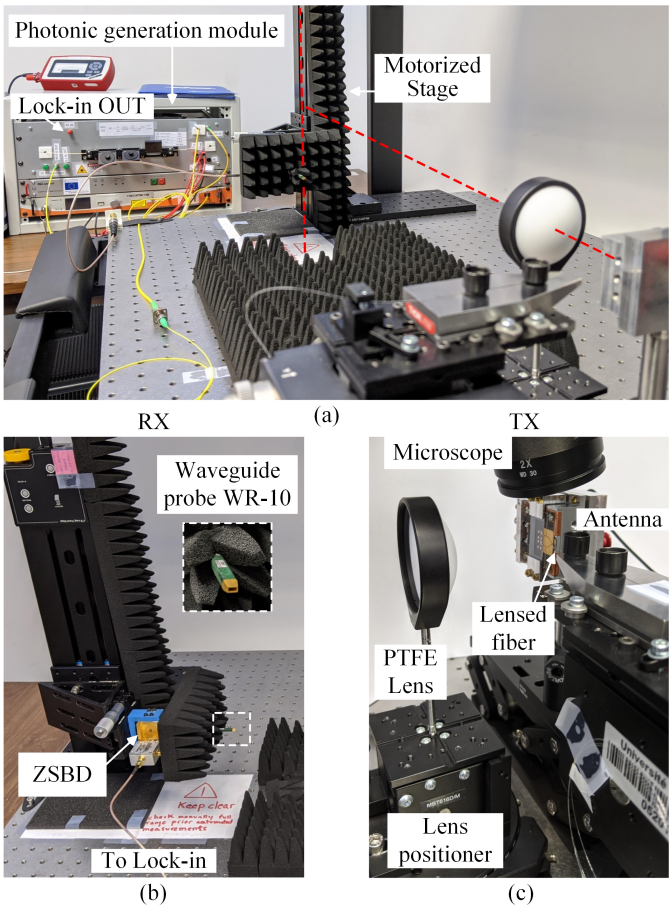

Fig. 9. Set-up used to characterize beam switching.

the antenna gain, and the measured and simulated results are shown in Fig. 7. A maximum deviation of 0.8 dB with respect to full-wave simulations is obtained, with measured gain values of 12.3 ± 0.7 dB between 75-87 GHz. The gain decrease in the upper end of the frequency window is due to an increased return loss (see Fig. 6). The estimated radiation efficiency is > 75 % at E-band frequencies.

IV. Photonic Beam Switching

To realize photonic beam switching, the antenna array is placed at the focal plane of a PTFE lens (Thorlabs LAT075) with a back focal length (bfl) of 53 mm and a diameter of 5 cm. The two sub-arrays lie symmetrically $s = 2.5$ mm above and below the optical axis (refer to Fig. 1b). From (1), excitation of one of either photodiodes produces a tilted beam at an angle $\theta = \pm 2.7°$, which would assist in fine beam alignment.

Fig. 8 shows the set-up schematic to characterize beam switching, and Fig. 9a shows the set-up mounted on an optical table. It enables radiation pattern measurements along a vertical cut. At the background of Fig. 9a, one observes the rack box containing the photonic generation module. This module hosts the blocks used for mm-wave generation by photomixing [42]: two fiber-coupled free-running laser diodes (Toptica Photonics DFB pro BFY), a fiber combiner, a Mach Zhender modulator (iXBlue MX-LN-20) with its driver (iXBlue DR-DG-20-MO),

a modulation bias controller that sets the modulator at the quadrature point (iXBlue MBC-DG-LAB), and a polarization controller. The photonic generation module outputs two amplitude modulated, $\approx 1.55\,\mu$m optical tones whose separation is the desired mm-wave frequency with an accuracy better than $10\,$MHz. The module input is an RF signal that modulates the output beatnote. For the beam switching experiment, a $100\,$kHz sinusoidal waveform from a lock-in amplifier (SRS SR830) connects to the module RF input (marked in Fig. 9a as Lock-in OUT). Next, the module output is directed by a fiber patchcord (depicted in yellow in Fig. 8) to a lensed fiber (OZ optics) that illuminates one of the two UTC-PDs in the chip. Precise alignment of the fiber to the optical input of the PD is enabled by a 3-axis micropositioner (Thorlabs Nanomax 313D with $50\,\mu\mathrm{m/rev.}$ positioning precision). At a distance corresponding to bfl from the antenna, the lens is placed and aligned with another positioner, as shown in Fig. 9c. The receiving side consists of a WR-10 waveguide probe (shown in Fig. 9b), in turn connected to a zero bias Schottky barrier diode detector (ZSBD) from VDI [46]. The ZSBD is mounted on a linear motorized translation stage (Thorlabs LTS300), denoted as motorized stage in Fig. 9a. This stage enables a 30 cm excursion range, and, together with the Lock-in amplifier, they are computer controlled for experiment automation. To avoid undesired reflections and standing waves, the optical table, translation stage, and receiving module are covered with absorber. Finally, to close the loop, the RF output of the ZSBD is extracted with a bias-tee connected to the Lock-in amplifier input, and the detected relative amplitude is measured. Lock-in amplification is used because the small electrical aperture of the waveguide probe captures little power. The measurement distance (waveguide probe tip to lens) is $d = 60.5\,$cm, which is a trade-off between angular coverage allowed by the translation range, signal level, and lens far-field ($1.15\,$m). The angular resolution of this detection scheme is $0.12°$.

The simulation results of the antenna plus lens (including the annular lens mount) using ANSYS HFSS' Finite Element-Boundary Integral (FE-BI) boundary conditions are shown in Fig. 10a for $75\,$GHz and in Fig. 10b for $85\,$GHz. The figures also show the measured values. The half-power beamwidths are $5.2°$ and $4.8°$, respectively, and the simulated directivities are $27.5\,$dBi and $27.9\,$dBi, respectively (the system does not allow directivity measurements but is expected to be in this range given that the curves are in very good agreement). For a separation between sub-arrays of $5\,$mm, the beam crossover occurs approximately at $-3\,$dB, as can be observed in Fig. 10. Furthermore, the pointing direction is stable within $\pm 0.1°$ across the E-band.

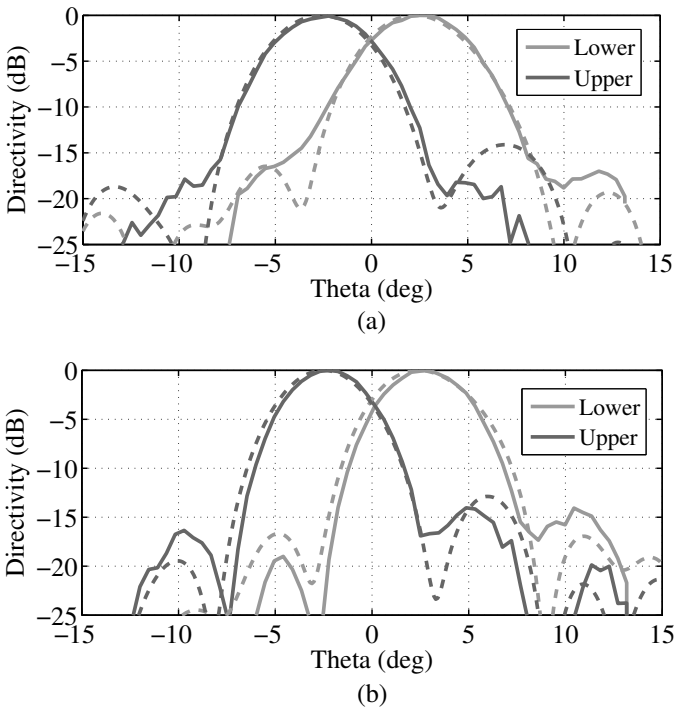

Fig. 10. Measured (continuous line) and simulated (dashed line) normalized radiation patterns versus elevation angle for the experimental characterization of photonic beam switching for (a) 75 GHz, and (b) 85 GHz. Lower and Upper refer to the sub-array position respect to the optical axis.

V. Wireless Link Demonstrations

Last, the photonic transmitter is tested in a wireless link. The experimental set-up is similar to that shown in Fig. 9. In this case, the waveguide probe is substituted by a waveguide horn and another $5\,$cm diameter PTFE lens. At the output of the ZSBD, a $42\,$dB gain amplifier (Wenteq ABL0300004030) plus a $10\,$dB gain block (Minicircuits ZX60-14012L-S+) are connected. Finally, the lock-in detector is replaced by an Anritsu MP1763C pulse pattern generator providing the RF input to the photonic generation module of Fig. 9a, and an Anritsu 1764C error detector.

Fig. 11a shows the bit-error rate (BER) versus the detector elevation angle when the upper or lower sub-arrays are active for a carrier at the lower frequency window in the E-band ($73\,$GHz). In turn, Fig. 11b depicts the same curve for a carrier in the higher frequency window ($83\,$GHz). Fig. 11c shows the eye diagram for optimum BER $= 10^{-11}$. The slight eye asymmetry could be attributed to saturation of the ZSBD and the subsequent RF amplification chain. The photocurrent is kept at $3.7\,$mA and the link distance is also $d = 60.5\,$cm. On-off keying modulation is used with a data rate of $5\,$Gbps, which is limited by the amplifier bandwidth ($3\,$GHz). Still, the link baud rate ($5\,$Gbaud/s) is double of that reported in [21] ($2.5\,$Gbaud/s) using a phased array and $16-$ QAM for a $50\,$cm distance. The curves in Fig. 11a and b show that, for both E-band windows, link operation is accomplished (BER $< 10^{-3}$) over an angular range approximately twice as wide with respect to a fixed beam. Thus, the developed Tx yields a system more tolerant to misalignment.

VI. Conclusion

We have demonstrated a broadband solution for beam switching with a photonic Tx at E-band for telecommunications. First, we have discussed the technique of photonic beam switching for photonic transmitters at mm- and sub-mm waves with a directive and flexible beam. Its advantages

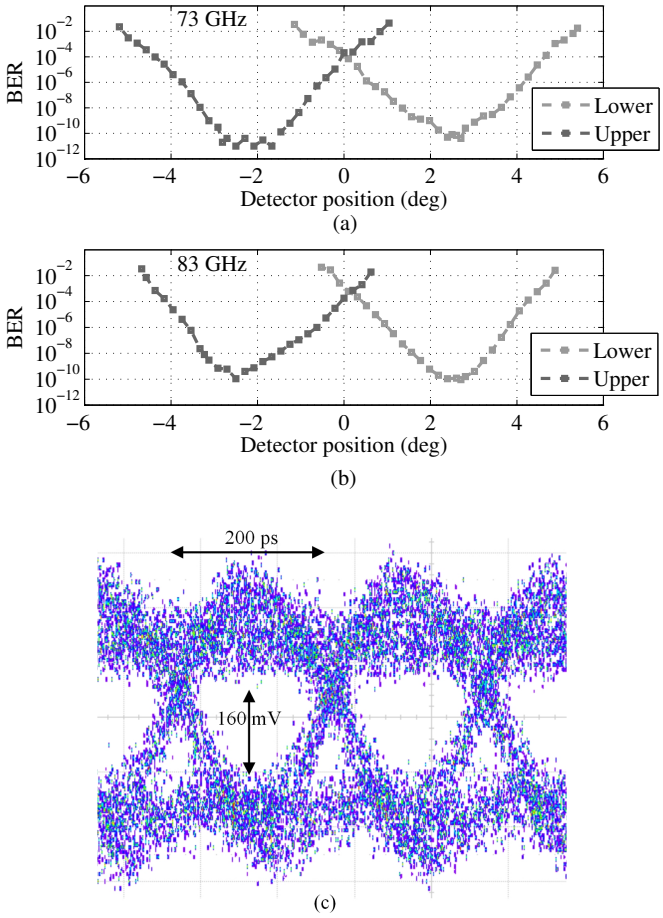

Fig. 11. (a) and (b): BER versus detector elevation angle for the upper and lower sub-arrays at the two windows of the E-band. (c) Eye diagram for BER= 10^{-11} with a 73 GHz carrier.

include a simple architecture for the distribution of optical power, the possibility of integrating a low number of active elements, and a directive beam. Next, we have presented the design, assembly, and validation of an antenna consisting of two 2×2 sub-arrays of stacked patches fed independently by two UTC-PDs. When the antenna is placed at the focal plane of a PTFE lens, excitation of one of either sub-arrays allows 1-D beam switching between $\pm 2.7°$ with a simulated directivity $> 27\,\mathrm{dBi}$. Finally, we have tested the transmitter in a wireless link. Depending on which sub-array is active and on the receiver position, live data transmission at $5\,\mathrm{Gbps}$ is achieved for a $60.5\,\mathrm{cm}$ link distance. The presented work sets the basis to develop more advanced designs of broadband photonic transmitters with a highly directive and switchable beam to overcome the tight alignment tolerances of point-to-point mm-wave wireless links.

ACKNOWLEDGMENT

The authors would like to thank X. Morvan (M^2ARS platform and Université de Rennes 1) for manufacturing the housing and to the NanoRennes platform (CNRS) for carrying out the photolithography and assembly operations. The authors are also grateful to III-V Labs for lending the photodiode chips used in this work.

REFERENCES

[1] J. G. Andrews *et al.*, "What will 5G be?" *IEEE J. Sel. Areas Commun.*, vol. 32, no. 6, pp. 1065–1082, 2014.
[2] H. Elayan, O. Amin, B. Shihada, R. M. Shubair, and M. S. Alouini, "Terahertz band: The last piece of RF spectrum puzzle for communication systems," *IEEE Open J. Comm. Soc.*, vol. 1, pp. 1–32, 2020.
[3] T. Nagatsuma and G. Carpintero, "Recent progress and future prospect of photonics-enabled Terahertz communications research," *IEICE Trans. Electron.*, vol. E98.C, no. 12, pp. 1060–1070, 2015.
[4] J. Ala-Laurinaho *et al.*, "2-D beam-steerable integrated lens antenna system for 5G E-band access and backhaul," *IEEE Trans. Microw. Theory Techn.*, vol. 64, no. 7, pp. 2244–2255, 2016.
[5] M. Frecassetti, "E-band and V-band -survey on status of worldwide regulation," *ETSI white paper*, no. 9, pp. 3495–3501, 2015.
[6] *Attenuation by atmospheric gases, Rec. ITU-R P.676-8*, International Telecommunications Union, Geneva, Switzerland, Sept. 2009.
[7] S. Jia *et al.*, "120 Gb/s multi-channel THz wireless transmission and THz receiver performance analysis," *IEEE Photon. Technol. Lett.*, vol. 29, no. 3, pp. 310–313, 2017.
[8] G. Carpintero *et al.*, "Microwave photonic integrated circuits for millimeter-wave wireless communications," *J. Lightw. Technol.*, vol. 32, no. 20, pp. 3495–3501, 2014.
[9] J. A. Altabas *et al.*, "Nonorthogonal multiple access and carrierless amplitude phase modulation for flexible multiuser provisioning in 5G mobile networks," *J. Lightw. Technol.*, vol. 35, no. 24, pp. 5456–5463, 2017.
[10] A. Hirata *et al.*, "120-GHz-band wireless link technologies for outdoor 10-Gbit/s data transmission," *IEEE Trans. Microw. Theory Techn.*, vol. 60, no. 3, pp. 881–895, 2012.
[11] A. Hirata, "Transmission trial of television broadcast materials using 120-GHz-band wireless link," NTT Microsystem Integration Laboratories, Tech. Rep., 2009.
[12] K. Sengupta, T. Nagatsuma, and D. M. Mittleman, "Terahertz integrated electronic and hybrid electronic-photonic systems," *Nat. Electron.*, vol. 1, pp. 622–635, 2018.
[13] D. Headland, Y. Monnai, D. Abbott, C. Fumeaux, and W. Withayachumnankul, "Tutorial: Terahertz beamforming, from concepts to realizations," *APL Photonics*, vol. 3, no. 5, p. 051101, 2018.
[14] A. J. Seeds, H. Shams, M. J. Fice, and C. C. Renaud, "Terahertz photonics for wireless communications," *J. Lightw. Technol.*, vol. 33, no. 3, pp. 579–587, 2015.
[15] S. Hur, T. Kim, D. J. Love, J. V. Krogmeier, T. A. Thomas, and A. Ghosh, "Millimeter wave beamforming for wireless backhaul and access in small cell networks," *IEEE Trans. Commun.*, vol. 61, no. 10, pp. 4391–4403, 2013.
[16] R. Kalimulin, A. Artemenko, R. Maslennikov, J. Putkonen, and J. Salmelin, "Impact of mounting structures twists and sways on point-to-point millimeter-wave backhaul links," in *2015 IEEE Int. Conf. Commun. Workshop (ICCW)*, 2015, pp. 19–24.
[17] S. Rommel, T. R. Raddo, U. Johannsen, C. Okonkwo, and I. T. Monroy, "Beyond 5G - wireless data center connectivity," in *Broadband Access Communication Technologies XIII*, B. B. Dingel, K. Tsukamoto, and S. Mikroulis, Eds., Int. Soc. Optics and Photonics. SPIE, 2019, pp. 125 – 133.
[18] N. Shimizu and T. Nagatsuma, "Photodiode-integrated microstrip antenna array for subterahertz radiation," *IEEE Photon. Technol. Lett.*, vol. 18, no. 6, pp. 743–745, 2006.
[19] S. Preu *et al.*, "Fiber-coupled 2-D n-i-pn-i-p superlattice photomixer array," *IEEE Trans. Antennas Propag.*, vol. 65, no. 7, pp. 3474–3480, 2017.
[20] Y. Zhou, G. Sakano, Y. Yamanaka, H. Ito, T. Ishibashi, and K. Kato, "600-GHz-wave beam steering by terahertz-wave combiner," in *2018 Optical Fiber Communications Conf. and Expo. (OFC)*, 2018, pp. 1–3.
[21] T. P. McKenna, J. A. Nanzer, and T. R. Clark, "Photonic beamsteering of a millimeter-wave array with 10-Gb/s data transmission," *IEEE Photon. Technol. Lett.*, vol. 26, no. 14, pp. 1407–1410, 2014.
[22] M. Che, Y. Matsuo, H. Kanaya, H. Ito, T. Ishibashi, and K. Kato, "Optoelectronic THz-wave beam steering by arrayed photomixers with integrated antennas," *IEEE Photon. Technol. Lett.*, vol. 32, no. 16, 2020.
[23] M. Steeg, P. Lu, J. Tebart, and A. Stöhr, "2D mm-wave beam steering via optical true-time delay and leaky-wave antennas," in *2019 12th German Microwave Conf. (GeMiC)*, 2019, pp. 158–161.
[24] J. Butler, "Beam-forming matrix simplifies design of electronically scanned antennas," *Electronic Design*, vol. 9, pp. 170–173, 1961.

[25] T. Djerafi and K. Wu, "A low-cost wideband 77-GHz planar Butler matrix in SIW technology," *IEEE Trans. Antennas Propag.*, vol. 60, no. 10, pp. 4949–4954, 2012.
[26] K. Tekkouk, J. Hirokawa, R. Sauleau, M. Ettorre, M. Sano, and M. Ando, "Dual-layer ridged waveguide slot array fed by a Butler matrix with sidelobe control in the 60-GHz band," *IEEE Trans. Antennas Propag.*, vol. 63, no. 9, pp. 3857–3867, 2015.
[27] W. Rotman and R. Turner, "Wide-angle microwave lens for line source applications," *IEEE Trans. Antennas Propag.*, vol. 11, no. 6, pp. 623–632, 1963.
[28] K. Tekkouk, M. Ettorre, L. Le Coq, and R. Sauleau, "Multibeam SIW slotted waveguide antenna system fed by a compact dual-layer Rotman lens," *IEEE Trans. Antennas Propag.*, vol. 64, no. 2, pp. 504–514, 2016.
[29] A. Attaran, R. Rashidzadeh, and A. Kouki, "60 GHz low phase error Rotman lens combined with wideband microstrip antenna array using LTCC technology," *IEEE Trans. Antennas Propag.*, vol. 64, no. 12, pp. 5172–5180, 2016.
[30] D. Filipovic, G. Gauthier, S. Raman, and G. Rebeiz, "Off-axis properties of silicon and quartz dielectric lens antennas," *IEEE Trans. Antennas Propag.*, vol. 45, no. 5, pp. 760–766, 1997.
[31] B. Rupakula, A. Nafe, S. Zihir, Y. Wang, T.-W. Lin, and G. Rebeiz, "63.5–65.5-GHz transmit/receive phased-array communication link with 0.5–2 Gb/s at 100–800 m and ± 50° scan angles," *IEEE Trans. Microw. Theory Tech.*, vol. 66, no. 9, pp. 4108–4120, 2018.
[32] A. Artemenko, A. Mozharovskiy, A. Sevastyanov, V. Ssorin, and R. Maslennikov, "Electronically beam steerable lens antenna for 71–76/81–86 GHz backhaul applications," in *2015 IEEE MTT-S Int. Microwave Symp.*, 2015, pp. 1–4.
[33] K. Tekkouk, M. Ettorre, E. Gandini, and R. Sauleau, "Multibeam pillbox antenna with low sidelobe level and high-beam crossover in SIW technology using the split aperture decoupling method," *IEEE Trans. Antennas Propag.*, vol. 63, no. 11, pp. 5209–5215, 2015.
[34] Agiltron. (2021) "1 x 4 high speed optical switch module - NanoSpeed". [Online]. Available: https://agiltron.com/product/ns-high-speed-optical-1x4-switch/.
[35] X. Fu, F. Yang, C. Liu, X. Wu, and T. J. Cui, "Terahertz beam steering technologies: From phased arrays to field-programmable metasurfaces," *Adv. Opt. Mater.*, vol. 8, no. 3, p. 1900628, 2020.
[36] O. Lafond and M. Himdi, "Printed millimeter antennas– multilayer technologies," in *Advanced Millimeter-Wave Technologies*, D. Liu, B. Gaucher, U. Pfeiffer, and J. Grzyb, Eds. Chichester, UK: John Wiley & Sons, Ltd, 2009, pp. 163–232.
[37] ANSYS, "High Frequency Structure Simulator," 2019, ver. 19.0.0.
[38] D. M. Pozar and D. Schaubert, Eds., *Microstrip antennas: the analysis and design of microstrip antennas and arrays*. Institute of Electrical and Electronics Engineers, 1995.
[39] M. Khalily, R. Tafazolli, P. Xiao, and A. A. Kishk, "Broadband mm-wave microstrip array antenna with improved radiation characteristics for different 5G applications," *IEEE Trans. Antennas Propag.*, vol. 66, no. 9, pp. 4641–4647, 2018.
[40] Heareus Conamic. (2021) Electrical properties of quartz. [Online]. Available: https://www.heraeus.com/en/hca/fused_silica_quartz_knowledge_base_1/properties_1/properties_hca.html
[41] E. Rouvalis *et al.*, "High-speed photodiodes for InP-based photonic integrated circuits," *Opt. Express*, vol. 20, no. 8, pp. 9172–9177, Apr 2012.
[42] A. J. Pascual *et al.*, "A photonically-excited leaky-wave antenna array at E-Band for 1-D beam steering," *Appl. Sci.*, vol. 10, no. 10, 2020.
[43] M. Ali, L. E. García Muñoz, and G. Carpintero, "E-band photonic transmitter with tapered slot antenna for RoF applications," in *2017 Int. Topical Meeting Microw. Photon. (MWP)*, 2017, pp. 1–4.
[44] M. Ali *et al.*, "300 GHz optoelectronic transmitter combinig integrated photonics and electronic multipliers for wireless communication," *Photonics*, vol. 6, no. 35, 2019.
[45] *Product selector guide Rev. 3*, Rogers Corp., 2020.
[46] Virginia Diodes. (n.d.) Zero bias detectors: Model WR10ZBD. [Online]. Available: https://www.vadiodes.com/en/wr10zbd